Analysis of RF Sheath-Driven Tungsten Erosion at RF Antenna in the WEST Tokamak

Atul Kumar[1,*], *Wouter* Tierens[1], *Tim* Younkin[1], *Curt* Johnson[1], *C. Christopher* Klepper[1], *Abdou* Diaw[1], *Jeremy* Lore[1], *Alex* Grosjean[2], *Guillaume* Urbanczyk[3], *Julien* Hillairet[4], *Patrick* Tamain[4], *Laurent* Colas[4], *Christophe* Guillemaut[4], *Davide* Curreli[5], *Syun'ichi* Shiraiwa[6], *Nicola* Bertelli[6], and The WEST Team[7]

[1]Oak Ridge National Laboratory, 1 Bethel Valley Road, Oak Ridge, TN-37831, USA
[2]University of Tennessee, Knoxville, TN 37996, USA
[3]Institut Jean Lamour UMR 7198 CNRS - Université de Lorraine, 2 allée André Guinier, F-54011 Nancy, France
[4]CEA, IRFM, F-13108 Saint-Paul-lez-Durance, France
[5]University of Illinois at Urbana-Champaign, Urbana, IL 61801, USA
[6]Princeton Plasma Physics Laboratory, Princeton, NJ 08536, USA
[7]http://west.cea.fr/WESTteam

Abstract. This study applies the newly developed STRIPE (Simulated Transport of RF Impurity Production and Emission) framework to analyze tungsten (W) erosion at RF antenna structures in the WEST tokamak. STRIPE integrates SolEdge3x for edge plasma backgrounds, COMSOL for 3D RF sheath potentials, RustBCA for sputtering yields, and GITR for impurity transport and ion energy–angle distributions. Building on prior work by Kumar et al. (2025) Nuclear Fusion, 65, 076039, which validated STRIPE for WEST ICRH discharge #57877, the present study provides a spatially resolved assessment of gross W erosion at both Q2 antenna limiters under ohmic and ICRH conditions. Simulations using 2D SolEdge3x profiles in COMSOL capture rectified sheath potentials exceeding 300 V, leading to strong upper-limiter localization. Both poloidal and toroidal asymmetries are observed and attributed to RF sheath effects, with modeled erosion patterns deviating from experiment—highlighting sensitivity to sheath geometry and plasma resolution. Erosion is driven primarily by high-charge-state oxygen ions (O^{6+}–O^{8+}), while D^+ plays a negligible role. Assuming a plasma composition of 1% oxygen and 98% deuterium, STRIPE predicts a 30-fold increase in gross W erosion from ohmic to ICRH phases, consistent with a >25-fold rise in W-I (400.9 nm) brightness. Quantitative agreement is within 5% in the ohmic phase and 30% under ICRH, demonstrating predictive capability. Importantly, the study shows that the magnitude of ICRH-driven W erosion depends strongly on the concentration of light impurities (O, B, N, C), which drive sputtering through high charge states. Cleaner plasma conditions with reduced impurity content are therefore expected to substantially mitigate antenna W sources in WEST and other toroidal fusion devices. These findings establish STRIPE as a predictive framework for RF-induced plasma–material interactions and support its application to reactor-scale antenna design.

1 Introduction

Radio-frequency (RF) waves are a primary tool for heating and current drive in magnetically confined fusion (MCF) plasmas [1]. With the move toward reactor-scale devices, such as SPARC [2], RF-based systems are expected to serve as primary heating sources, further motivating the need to understand associated edge plasma effects. One major concern in high-power RF operation is the formation of rectified RF sheaths at plasma-facing components (PFCs), particularly near ICRH antenna structures. Driven by RF waves, these sheaths can sustain potentials of several hundred volts in existing devices [3] and are projected to exceed 1 kV in future systems such as ITER [4]. Sheath-accelerated ions, including fuel species and light impurities, can induce physical sputtering of antenna materials—typically high-Z metals like tungsten (W). The resulting impurity sources can enter the scrape-off layer (SOL), and under certain conditions, migrate toward the core plasma. This is especially problematic in H-mode regimes, where longer confinement times enhance impurity retention and degrade overall performance.

Localized impurity generation driven by RF sheath rectification has been observed in toroidal devices [5]. While mitigation strategies such as changing antenna power balance ratio and the strap phasing [6], wall conditioning [7], and field-aligned launchers [8] have shown limited success. Moreover, only a few initial efforts have

*Corresponding author: kumara@ornl.gov

This manuscript has been authored by UT-Battelle, LLC, under contract DE-AC05-00OR22725 with the US Department of Energy (DOE). The US government retains and the publisher, by accepting the article for publication, acknowledges that the US government retains a nonexclusive, paid-up, irrevocable, worldwide license to publish or reproduce the published form of this manuscript, or allow others to do so, for US government purposes. DOE will provide public access to these results of federally sponsored research in accordance with the DOE Public Access Plan (http://energy.gov/downloads/doe-public-access-plan).

been made to modeled RF-induced PMI in detail [9, 10]. Nevertheless, the fusion community continues to seek predictive, integrated tools capable of linking RF field structure, edge plasma conditions, and impurity sourcing.

In this work, the newly developed STRIPE (Simulated Transport of RF Impurity Production and Emission) framework [11] is applied to assess W-erosion from the ICRH antenna limiters in the WEST tokamak for a dedicated L-mode ICRH discharge (#57877). WEST, with its all-W-PFCs and recently demonstrated record long-pulse operation capability exceeding 1300 seconds and injected energy of 2 GJ [12], provides a relevant platform for validating high-fidelity plasma-material interaction (PMI) models under reactor-relevant conditions.

In contrast to previous work on this discharge [11], which focused on validating STRIPE against localized W emission near the antenna region, this study presents a spatially resolved, in-depth analysis of plasma conditions and gross W-erosion to address experimentally observed erosion hot spots with both toroidal and poloidal asymmetries at the right and left antenna limiters. While STRIPE also supports modeling of redeposition, self-sputtering, and net erosion, those aspects are deferred to a companion study focused on whole-device transport of W-impurities originating from the ICRH antenna.

The remainder of this paper is structured as follows: Section 2 introduces the STRIPE framework and discusses main inputs to STRIPE framework. Section 3 presents results comparing thermal and RF sheath-driven erosion at the WEST ICRH limiters. Conclusions are summarized in Section 4.

2 Overview and Inputs of the STRIPE Framework

STRIPE (Simulated Transport of RF Impurity Production and Emission) [11] is an integrated, multi-physics framework developed to model impurity-driven W erosion at ICRH antenna structures. It couples 2D edge plasma backgrounds from SolEdge3x [13], rectified RF sheath potentials from COMSOL [3], ion trajectory and impact dynamics from GITR [14] and RustBCA [15], and post-processing via ColRadPy [16] to convert sputtered fluxes into spectroscopically observable emission.

The STRIPE workflow (Fig. 1) enables predictive modeling of RF-enhanced PMI by integrating sheath fields, charge-resolved impurity fluxes, and energy–angle-dependent sputtering yields. In this study, STRIPE is applied to model W erosion at the WEST Q2 ICRH antenna for discharge #57877 under both ICRH and ohmic conditions.

The framework relies on spatially resolved physics inputs that capture gradients in plasma parameters, impurity species, and sheath voltages across 3D limiter geometries. These include SolEdge3x-derived electron density and temperature profiles, COMSOL-calculated sheath fields, and surface interaction data from RustBCA. The following subsections present these key inputs and how they are incorporated to simulate limiter-targeted impurity production and erosion.

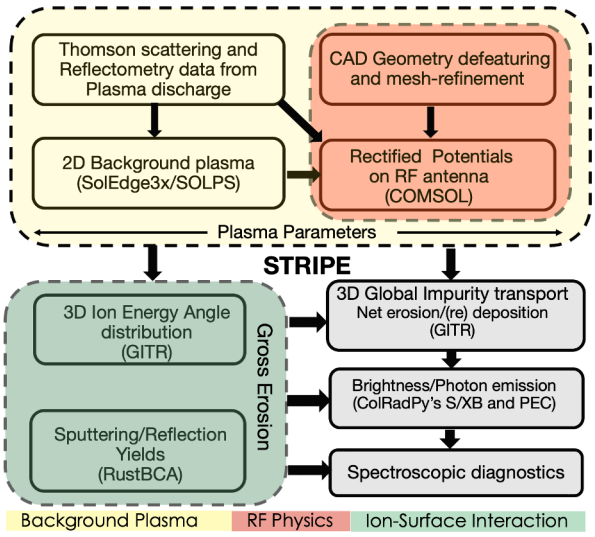

Figure 1. STRIPE workflow for modeling W erosion and impurity transport originating from ICRH antenna structures, coupling SolEdge3x, COMSOL, RustBCA, GITR, and ColRadPy.

2.1 Limiter-Resolved Plasma Profiles and Charge State Distribution

Figure 2 shows the time evolution of key plasma parameters for WEST discharge #57877, which serves as the experimental basis for the SolEdge3x simulations used in this study. The discharge begins with ohmic heating from $t = 0$ to 5 s and transitions to ICRH at $t = 5$ s, with a total power input of approximately 2.3 MW, including 1.7 MW delivered through the Q2 antenna. Panel (b) displays the visible brightness of the W I line, averaged over lines of sight viewing both the antenna limiters and the inner and outer divertor strike points.

Visible spectroscopy for this discharge reveals distinct poloidal variations in W emission across PFCs. As shown in Figure 2(b), the inner divertor exhibits strong W I emission during the ohmic phase—when the leg is attached—but this signal vanishes just before ICRF turn-on, consistent with detachment. Conversely, the outer divertor shows reduced emission during the ohmic phase, followed by a transient W I peak at ICRF initiation that subsequently decays during the power flat-top, possibly due to evolving sheath conditions or partial detachment. In contrast, the antenna region sustains elevated W I emission throughout the ICRH phase, consistent with enhanced RF sheath-driven erosion. Notably, W I brightness from the antenna increases by a factor of ~25 during transition from ohmic to ICRH phase.

Although the global radiated power fraction $P_{\mathrm{rad}}/P_{\mathrm{in}}$ remains nearly unchanged between ohmic and ICRH phases (Figure 2(a)), this global metric masks important spatial variations in impurity sourcing. In particular, increased tungsten emission near the antenna may be compensated by reduced divertor contributions—an effect also reported in recent WEST experiments [17]. A more detailed discussion of this behavior and its implications for W transport and balance is provided in Section 4.

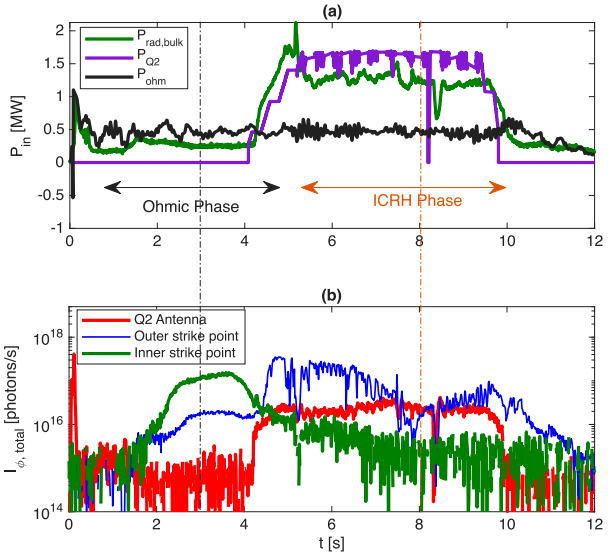

Figure 2. Time evolution of (a) heating power from ohmic and Q2 ICRH systems, together with total radiated power; (b) W-I 400.9 nm brightness measured along lines of sight viewing the antenna limiters and the inner and outer divertor strike points. The transition from ohmic to ICRH results in a strong rise in W-emission, with the antenna signal increasing by nearly a factor of 25–30.

Background SOL plasma conditions are reconstructed using wide-grid SolEdge3x–EIRENE simulations at two representative time points: $t = 3$ s (ohmic phase) and $t = 8$ s (ICRH phase). The simulation setup and boundary conditions are described in detail in [11]. These 2D edge plasma solutions span the entire SOL and provide spatially resolved plasma parameters adjacent to the antenna-facing surfaces. In the present simulations, plasma composition is set to 99% deuterium (D^+) and 1% oxygen (O), with O serving as a proxy for all light impurities present during this WEST discharge. The O total density is fixed at 1% of the electron density, initialized uniformly from the core boundary and assumed spatially homogeneous. This simplification captures impurity behavior and radiative cooling effects reasonably well, as O concentrations in WEST are typically observed to lie between 0.1% and 10% [9, 18]. The implication of this assumption on W-source is discussed later in Section 4.

In SolEdge3x, the wall geometry is modeled as toroidally symmetric, whereas the actual WEST ICRH antenna exhibits a pronounced poloidal asymmetry about the midplane. This geometric simplification can reduce the fidelity of local plasma representation near the antenna and partly explain discrepancies between STRIPE predictions and experimental impurity emission. To isolate the role of RF sheath rectification on tungsten erosion, drifts are disabled and identical transport coefficients are applied in both ohmic and ICRH phases. Although RF sheath rectification is expected to modify local transport—for example, by driving $\mathbf{E} \times \mathbf{B}$ convective cells from gradients in the rectified DC potential—these effects are deliberately excluded here so that impurity sourcing can be attributed primarily to variations in sheath potential rather than changes in radial transport. The possible contribution of such RF-driven cross-field convection is addressed in Section 4.

Figure 3 compares the SolEdge3x-predicted electron density (n_{e^-}) with outer midplane (OMP) reflectometry measurements for WEST discharge #57877 during the ICRH phase. The simulation shows good agreement with experimental data in the radial region of interest. The corresponding simulated electron temperature (T_{e^-}) profile is also shown. However, no reliable T_{e^-} measurements are available during the ICRH phase, and no data were collected during the ohmic phase.

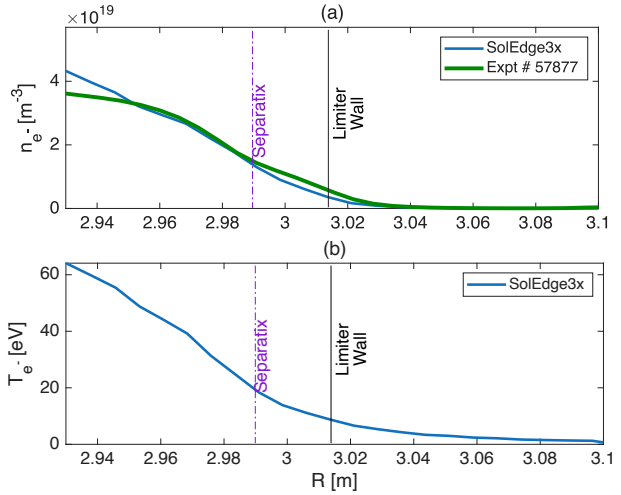

Figure 3. Radial profiles of (a) electron density n_{e^-} and (b) electron temperature T_{e^-} at the OMP SOL from SolEdge3x simulations during the ICRH phase ($t = 8$ s). The n_{e^-} profile is compared with reflectometry data from WEST discharge #57877, showing reasonably good agreement in the SOL and far-SOL region.

Profiles of n_{e^-} and T_{e^-} are mapped along 3D limiter-facing surfaces and then averaged over synthetic line-of-sight (LOS) chords, consistent with both the spectroscopic diagnostic geometry and the STRIPE mesh structure. This approach ensures that simulation inputs remain aligned with the spatial resolution and view factors of experimental diagnostics. Figures 4 and 5 present LOS-weighted vertical profiles of oxygen ion parameters obtained from SolEdge3x for the four highest charge states (O^{5+} to O^{8+}), including density $n_{O^{q+}}$, temperature $T_{O^{q+}}$, and particle flux $\Gamma_{O^{q+}}$ along the left (L) and right (R) Q2 antenna limiters.

ICRH Phase: During ICRH operation, as shown in Figure 4, the impurity population near both limiters is dominated by O^{6+}, O^{7+}, and O^{8+}. On the R limiter, $n_{O^{6+}}$ peaks near the midplane at approximately 3.0×10^{15} m^{-3}, while O^{8+} reaches about 2.5×10^{15} m^{-3}, and O^{7+} slightly less, at approximately 2.0×10^{15} m^{-3}, with peak values of all three charge states occurring in the upper region ($z > 0.1$ m). The contribution from O^{5+} is negligible throughout the profile.

The vertical distribution of oxygen charge states reflects the local T_{e^-} and ionization equilibrium. As shown in Figure 4, the effective ion temperatures $T_{O^{q+}}$ vary only

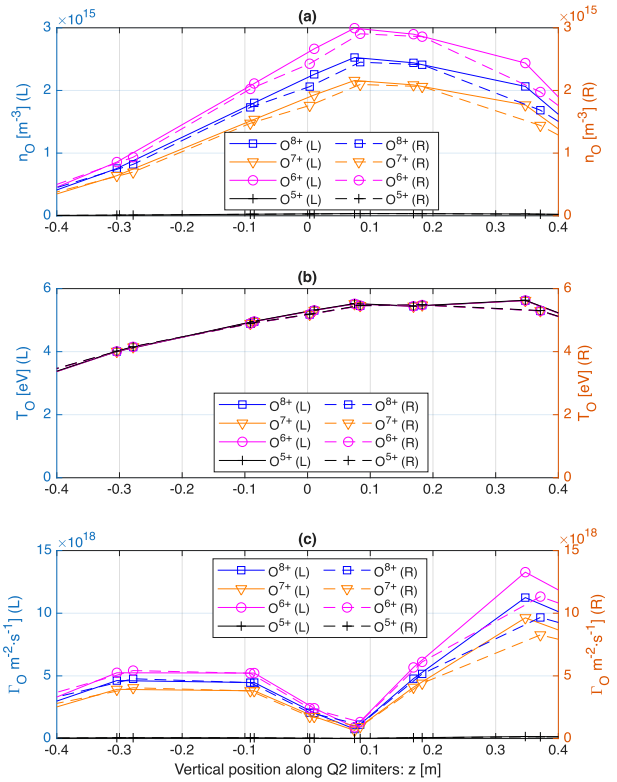

Figure 4. LOS-averaged vertical plasma profiles during the ICRH phase: (a) charge-resolved O ion densities $n_{O^{q+}}$; (b) corresponding temperatures $T_{O^{q+}}$; (c) particle fluxes $\Gamma_{O^{q+}}$. Profiles show stronger localization and a pronounced midplane dip.

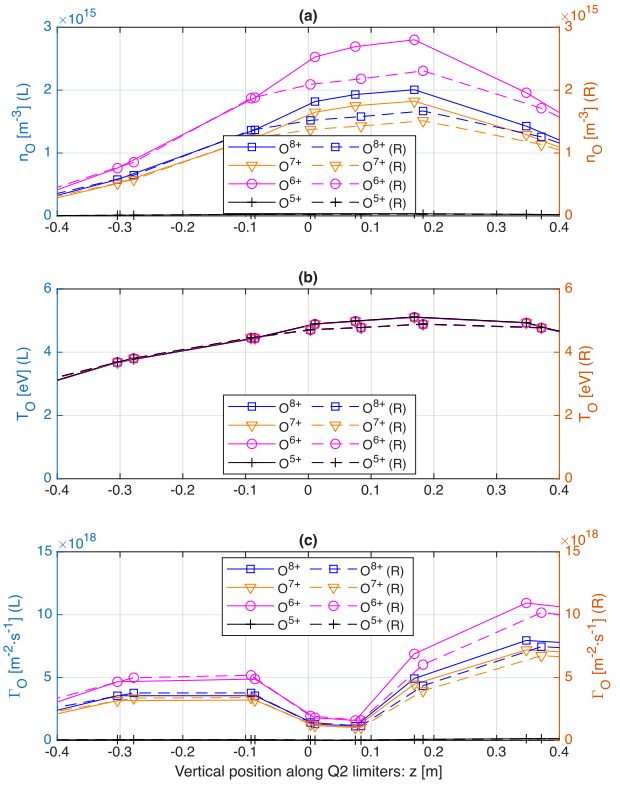

Figure 5. LOS-averaged vertical plasma profiles during the ohmic phase: (a) charge-resolved O ion densities $n_{O^{q+}}$; (b) corresponding temperatures $T_{O^{q+}}$; and (c) particle fluxes $\Gamma_{O^{q+}}$. The profiles are approximately symmetric across the midplane and show broad vertical distributions as compared to the ICRH case.

weakly across charge states, remaining in the range of 4–6 eV. In contrast, the flux profiles $\Gamma_{O^{q+}}$ exhibit pronounced vertical asymmetry. On the R limiter, $\Gamma_{O^{6+}}$, $\Gamma_{O^{7+}}$, and $\Gamma_{O^{8+}}$ all peak sharply in the upper region ($z \sim 0.3$–0.35 m), with $\Gamma_{O^{6+}}$ reaching values above 1.2×10^{19} m^{-2} s^{-1}. A distinct dip occurs near the midplane ($z = 0$), arising from the tangential magnetic field orientation and stagnation of parallel plasma flow, which reduce the local ion flux to the surface. On the L limiter, the vertical shapes of the flux profiles are similar, though the absolute magnitudes are systematically higher across all charge states. This asymmetry likely originates from the intrinsic geometric asymmetry of the WEST ICRH antenna, whereas the toroidal profiles remain nearly symmetric due to the axisymmetric wall geometry assumed in SolEdge3x. Small differences between the L and R limiter profiles may also reflect variations in LOS view chords for the corresponding diagnostics. The observed vertical localization of impurity fluxes coincides with regions of enhanced rectified sheath potentials predicted by COMSOL (Section 2.2), reinforcing the role of RF sheath rectification as a primary driver of erosion asymmetry.

Ohmic Phase: Under ohmic conditions, the overall impurity density remains comparable to that in the ICRH phase, but the relative charge state distribution shifts slightly as can be infered from Figure 5. Due to the marginally lower oxygen temperatures ($T_{O^{q+}} \sim$ 4.5–5.0 eV), O^{6+} becomes the most abundant species across both limiters. On the L limiter, peak $n_{O^{6+}}$ reaches approximately 2.8×10^{15} m^{-3}, while O^{8+} and O^{7+} reach about 2.0×10^{15} m^{-3} and 1.8×10^{15} m^{-3}, respectively. These charge states follow similar spatial distributions on the R limiter. O^{5+} remains weakly populated, consistent with limited ionization in the cooler peripheral regions.

Temperatures $T_{O^{q+}}$ remain relatively flat and symmetric along the vertical axis during the ohmic phase (Fig. 5b). The corresponding fluxes $\Gamma_{O^{q+}}$ exhibit broad vertical distributions with no pronounced midplane dip, in clear contrast to the ICRH case. Among the charge states, $\Gamma_{O^{6+}}$ dominates, reaching peaks near 1.2×10^{19} m^{-2} s^{-1}, while $\Gamma_{O^{7+}}$ and $\Gamma_{O^{8+}}$ remain below 0.7×10^{19} m^{-2} s^{-1}. The L- and R-limiter profiles are approximately symmetric, and the broader vertical distributions in the ohmic phase yield more uniform impurity exposure across limiter surfaces. This contrasts with the ICRH phase, where profiles are more localized and exhibit a pronounced midplane dip which may lead to stronger spatially localized erosion hotspots, as discussed further in Section 3.

2.2 RF-Rectified DC Sheath Potentials from Full-Wave COMSOL Simulations

Rectified sheath potentials induced by RF fields are essential boundary inputs to the STRIPE framework and are computed using full-wave electromagnetic simulations in

COMSOL Multiphysics. These simulations employ the sheath-equivalent dielectric layer method [3], which introduces thin layers of spatially varying complex permittivity and conductivity adjacent to PFCs. These material properties are derived from local plasma conditions, enabling the solution of Maxwell's equations under the cold plasma approximation to self-consistently capture RF field penetration and sheath rectification across realistic 3D geometries.

Input profiles for n_{e^-} and T_{e^-} are taken directly from SolEdge3x simulations, utilizing the wide-grid configuration described in Section 2.1. Unlike the previous approach in reference [3, 11] requiring extrapolation to cover the full RF-antenna components, this implementation benefits from full spatial resolution of the antenna-facing domain—including recessed Faraday Screen bars and antenna sidewalls—facilitating seamless integration into the COMSOL domain.

Figure 6 presents the computed 3D distribution of the rectified DC sheath potential $V_{\text{sheath}}^{\text{RF}}$ for WEST discharge #57877. Strong vertical asymmetries are evident, with voltages exceeding 350 V concentrated near upper part of antenna limiters' front and sidewalls. In contrast, lower regions exhibit significantly reduced voltages, typically below 100 V. These variations stem from the interplay between RF strap phasing, magnetic field topology, and nonuniform plasma conditions near the antenna aperture. Importantly, such large DC sheath potentials have also been *directly measured* in WEST using a reciprocating emissive probe, as reported in reference [19] which will be used in future for validating STRIPE's RF sheath predictions.

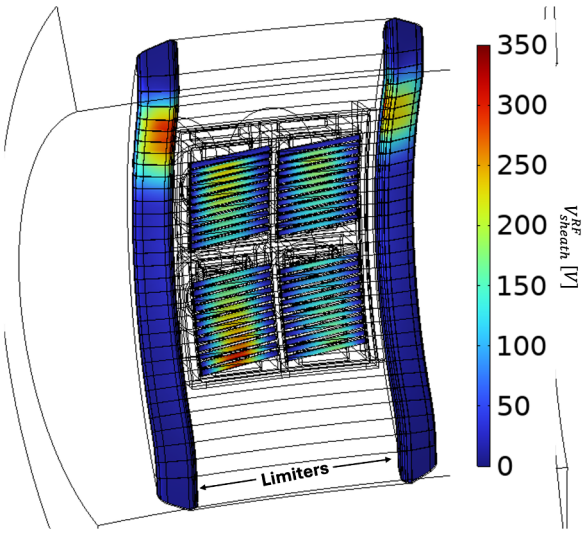

Figure 6. 3D map of rectified DC sheath potential $V_{\text{sheath}}^{\text{RF}}$ computed using COMSOL for WEST discharge #57877. Peak voltages exceed 250 V and are concentrated near the upper sections antenna limiters' front and sidewalls.

To further illustrate these trends, Figure 7 presents 1D vertical profiles of the peak $V_{\text{sheath}}^{\text{RF}}$ along the front face of the left and right Q2 antenna limiters during ICRH. Both profiles show pronounced vertical asymmetry, with peak rectified potentials localized near the upper ends, well above the midplane. In contrast, thermal sheath potentials during the ohmic phase are symmetric and centered around the midplane, with peak values near 25 V.

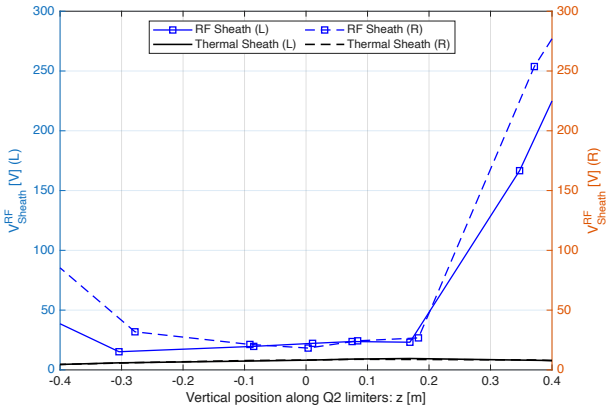

Figure 7. Peak $V_{\text{sheath}}^{\text{RF}}$ profiles along left and right Q2 limiters during ICRH in WEST #57877. Voltages exceed 200 V near the top; thermal sheath potentials (black) shown for reference.

Although n_{e^-} for the discharge #57877 remains well above the lower-hybrid resonance (LHR) cutoff, future cases closer to the LHR threshold may exhibit stronger slow-wave coupling and intensified sheath rectification—conditions to be investigated in upcoming COMSOL studies. The present model uses a local sheath formulation and does not include DC current equilibration along magnetic field lines. While such currents are treated in SSWICH, recent studies suggest its results align closely with those from Petra-M, which, like STRIPE, employs purely local sheath physics [20]. Notably, due to the magnetic field orientation, field-aligned equilibration would not eliminate toroidal asymmetries.

2.3 Ion-Surface Interaction and Erosion Modeling

STRIPE computes gross W-erosion by combining sheath-modified ion impact dynamics with angle- and energy-resolved sputtering yields. This process involves four key components: electric field modeling, ion trajectory integration, IEAD construction, and effective sputtering yield calculation.

Electric Field Profile: The local sheath electric field $E_n(r)$ is defined using an analytical model adapted from Brooks' formulation [21]:

$$E_n(r) = V_{\text{sheath}}\left[\frac{f_{\text{D}}}{2\lambda_{\text{D}}}\exp\left(-\frac{r}{2\lambda_{\text{D}}}\right) + \frac{1-f_{\text{D}}}{\rho_i}\exp\left(-\frac{r}{\rho_i}\right)\right], \quad (1)$$

where V_{sheath} voltage arising on the antenna structures due the sheath, r is the distance from the surface, λ_{D} is the Debye length, ρ_i is the ion gyroradius, and f_{D} is the fraction of the potential drop across the Debye sheath.

In ICRH phase, $V_{sheath} = V^{RF}_{sheath}$ is taken from COMSOL simulations detailed in subsection 2.2. For the ohmic phase, classical thermal sheath potentials $V_{sheath} = V^{Thermal}_{sheath}$ [22] are calculated as:

$$V^{thermal}_{sheath} = k_{sheath} T_e \,, \tag{2}$$

$$k_{sheath} = \left| \frac{1}{2} \log\left(2\pi \frac{m_e}{m_i}\right) \right| \left(1 + \frac{T_i}{T_e}\right), \tag{3}$$

where T_e and T_i are the electron and ion temperatures, and m_e, m_i are their respective masses.

Ion energy–angle distributions (IEADs): In STRIPE, IEADs, $f_i(\mathcal{E}, \theta)$, are computed by tracing impurity ion trajectories from the sheath entrance to the material surface using the GITR code. At each mesh element, 20,000 test particles are launched from the sheath entrance with a half-Maxwellian distribution. The local plasma parameters—n_{e^-}, T_{e^-}, n_{D^+}, T_{D^+}, $n_{O^{q+}}$, $T_{O^{q+}}$—together with electric (**E**) and magnetic (**B**) fields and the sheath potential (V_{sheath}), define the boundary conditions. Ion motion includes full gyromotion, $\mathbf{E} \times \mathbf{B}$ drift, and Coulomb collisions.

A limitation of the present approach is that GITR employs static sheath potentials and does not capture the fast time variation of the RF cycle. This simplification may affect the detailed shape of IEADs, particularly in the high-energy and grazing-angle tails. While adequate for estimating time-averaged erosion, the method may underestimate transient effects linked to sub-cycle RF dynamics. In principle, such effects could be addressed with fully kinetic approaches such as the hPIC code [23]; however, applying these methods to resolve the full 3D antenna geometry remains computationally expensive.

Sputtering yields for O ions incident on W, $Y(\mathcal{E}, \theta)(O \rightarrow W)$, or simply $Y(\mathcal{E}, \theta)$, are precomputed using RustBCA. A database of monoenergetic, angle-resolved simulations is generated for neutral atomic O impacting W, spanning ion energies $\mathcal{E}$ from 10 eV to 5 keV and incidence angles θ from 0° to 90°. Here, θ is defined as the angle between the ion velocity vector and the surface normal, such that $\theta = 0°$ corresponds to normal incidence and $\theta = 90°$ to grazing incidence. As in other BCA codes, RustBCA assumes neutral projectiles and does not account for long-range Coulomb interactions or charge-state-dependent stopping. This approximation is reasonable near material surfaces, where incident ions are expected to neutralize before impact.

Figure 8 summarizes the sputtering yield database. Panel (a) shows the angular dependence of $Y(\mathcal{E}, \theta)$ for selected ion energies, where yields increase with θ, peak between 70°–80°, and drop sharply near grazing incidence due to reflection. Panel (b) shows the energy dependence at fixed angles, where yields rise monotonically with $\mathcal{E}$ and exceed 2 atoms/ion at 5 keV for large θ. The color-coded legends indicate the specific values of $\mathcal{E}$ (top) and θ (bottom) used in the simulations, enabling direct interpretation of angular and energetic scaling.

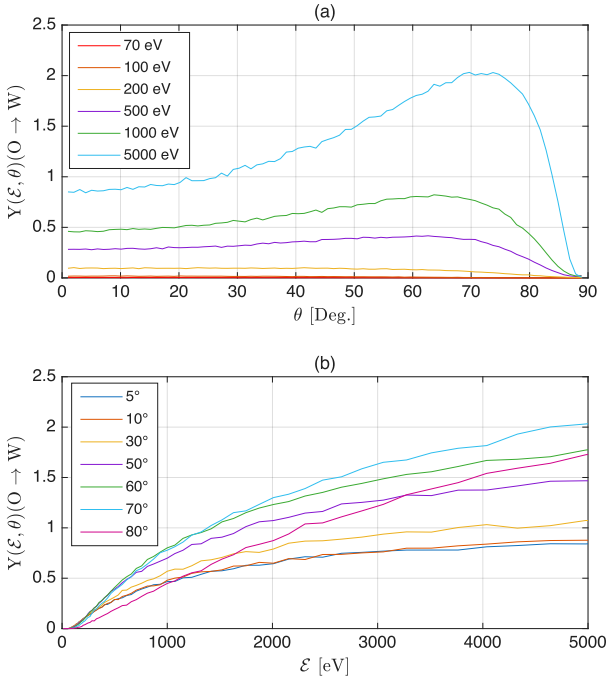

Figure 8. Sputtering yield $Y(\mathcal{E}, \theta)$ for neutral oxygen atoms incident on W, calculated using RustBCA. (a) Yield vs. incidence angle θ for selected ion energies: 70 eV (red), 100 eV (orange), 200 eV (gold), 500 eV (purple), 1000 eV (green), 5000 eV (blue). (b) Yield vs. ion energy $\mathcal{E}$ for selected incidence angles: 5°, 10°, 30°, 50°, 60°, 70°, 80°. By definition, $\theta = 0°$ corresponds to normal incidence and $\theta = 90°$ to grazing incidence.

The effective sputtering yield at each surface element is then obtained by convolving the GITR-computed IEADs with the RustBCA yield tables:

$$Y_{eff}(i) = \int_0^{90^\circ} \int_{\mathcal{E}_{min}}^{\mathcal{E}_{max}} Y_i(\mathcal{E}, \theta) f_i(\mathcal{E}, \theta)\, d\mathcal{E}\, d\theta. \tag{4}$$

Gross Erosion Flux: Effective yields $Y_{eff}(i)$ are combined with ion fluxes $\Gamma_{ions}(i)$ from SolEdge3x to compute the gross W erosion flux $\Gamma_{gross,W}$:

$$\Gamma_{gross,W} = \sum_{i=1}^{N} Y_{eff}(i) \cdot \Gamma_{ions}(i)\,. \tag{5}$$

This erosion flux serves as the impurity source for upstream modeling and synthetic diagnostics within STRIPE (see Section 3).

3 Results: W Erosion at the WEST ICRH Antenna Limiters

This section presents LOS-averaged vertical profiles of Y_{eff} and $\Gamma_{gross,W}$ on the L and R Q2 antenna limiters for WEST discharge #57877. STRIPE simulations are analyzed for three regimes: (i) ICRH phase with RF sheath, (ii) ICRH phase with thermal sheaths only, and (iii) ohmic phase. Particular attention is given to poloidal and toroidal asymmetries, and to the consistent presence of a midplane dip in erosion and brightness patterns.

3.1 ICRH Phase: RF Sheath Case

Figure 9 shows LOS-averaged profiles of Y_{eff} and $\Gamma_{\text{gross,W}}$ under ICRH conditions with RF sheath potentials included. The RF sheath voltage, computed using full-wave COMSOL simulations (see Section 2.2), reach peak values exceeding 300 V near the upper limiter surfaces, corresponding to regions with strong field-normal incidence and elevated O^{q+} fluxes.

Poloidal Trends: Y_{eff} for O^{6+}, O^{7+} and O^{8+}, reaches maximum values near $z \sim 0.34$ m (Figure 9a), coinciding with the region of highest rectified sheath potential. $\Gamma_{\text{gross,W}}$ exhibits a strongly localized erosion peak at the top of the L limiter, with $\Gamma_{\text{gross,W}}$ exceeding 5×10^{18} m^{-2} s^{-1} as shown in Fig 9b. This sharp localization indicates a synergy between localized sheath potentials and poloidally asymmetric impurity fluxes. A pronounced dip at the midplane (z = 0) is also observed, where erosion fluxes drop by more than an order of magnitude. This midplane suppression results from both reduced sheath potential and more tangential magnetic field orientation, which limit the energy and normal incidence of incoming ions. The combination of these effects leads to a highly non-uniform poloidal erosion profile, with strong localization of W sputtering near the upper limiter surface.

Toroidal Trends: The L limiter exhibits higher Y_{eff} than the R limiter in the upper region ($z > 0.18$ m), where yields from O^{8+} and O^{7+} are strongly localized. In contrast, the R limiter shows slightly elevated yields in the lower region ($z < 0$ m). Similar trends are observed in $\Gamma_{\text{gross,W}}$: the L limiter displays a pronounced peak near the top of the profile, while the R limiter presents a broader distribution with relatively enhanced erosion flux toward the bottom. Although the overall vertical shapes of the profiles are comparable between the two limiters, differences in magnitude and spatial localization result in a clear net toroidal asymmetry. This asymmetry reflects subtle variations in impurity flux distribution (Figure 9) and pronounced differences in local RF sheath potential exposure (Fig. 7), consistent with the erosion patterns predicted by STRIPE.

3.2 ICRH Phase: Thermal Sheath Case

To isolate the impact of RF rectification, STRIPE simulations were also performed for the ICRH phase using only thermal sheath potentials, with a peak sheath voltage of approximately 25 V.

Poloidal Trends: As shown in Figure 10(a), Y_{eff} on the R limiter exhibits a clear central peak at z = 0, consistent with the centrally peaked $V_{\text{sheath}}^{\text{Thermal}}$ and $n_{O^{q+}}$ in this regime. On the L limiter, the peak in Y_{eff} is slightly shifted upward to z $\sim$ 0.18 m, introducing a mild poloidal asymmetry. Across both limiters, the highest yields are observed for O^{8+} and O^{7+}, reaching up to 3.5×10^{-3}.

The corresponding $\Gamma_{\text{gross,W}}$, shown in Figure 10(b), follows a similarly broad poloidal distribution. On both R & L limiters, $\Gamma_{\text{gross,W}}$ increases monotonically toward the upper limiter edge. A *distinct midplane dip*, characteristic of the RF sheath case, is not evident here. The absence of

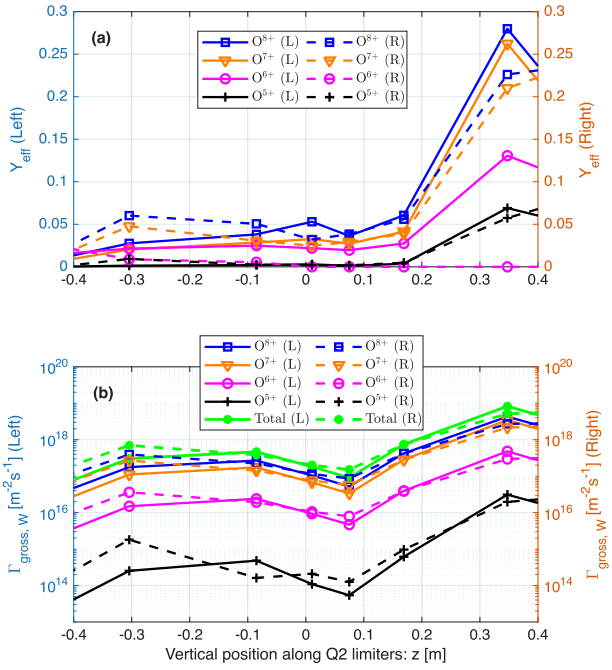

Figure 9. LOS-averaged vertical profiles during ICRH phase with RF sheath: (a) effective sputtering yield Y_{eff} for O^{q+} (q = 5–8); (b) gross erosion flux $\Gamma_{\text{gross,W}}$. Solid lines: L limiter; dashed lines: R limiter. A pronounced midplane dip is observed in both limiters.

strong vertical gradients reflects the more symmetric nature of the thermal sheath under non-rectified conditions.

Toroidal Trends: The L limiter continues to exhibit slightly higher erosion than the R limiter, although the asymmetry is moderate. Overall, the poloidal and toroidal erosion structure is more uniform in this case, reinforcing that the sharp localization seen under RF sheath conditions is driven primarily by sheath rectification effects.

3.3 Ohmic Phase

Erosion predictions during the ohmic phase are shown in Figure 11, where RF fields are absent and impurity fluxes are significantly reduced.

Poloidal Trends: The Y_{eff} and $\Gamma_{\text{gross,W}}$ profiles exhibit distinct poloidal characteristics on the L and R limiters. On the L limiter, Y_{eff} increases monotonically with vertical position and peaks slightly above the midplane, around z $\sim$ 0.18 m, indicating a spatial shift from the geometric center. The corresponding $\Gamma_{\text{gross,W}}$ profile rises steadily across the vertical extent and reaches its maximum near the upper end of the limiter. In contrast, the R limiter exhibits a non-monotonic Y_{eff} profile, with two local maxima at z $\sim$ 0 m and z $\sim$ 0.18 m, and a shallow local minimum near z $\sim$ 0.1 m. The erosion flux $\Gamma_{\text{gross,W}}$ on the R limiter reflects a similar vertical pattern, with relatively enhanced values toward the lower edges. These subtle but measurable poloidal variations influence the local erosion response even under symmetric thermal sheath conditions and reflect differences in local impurity transport and limiter geometry.

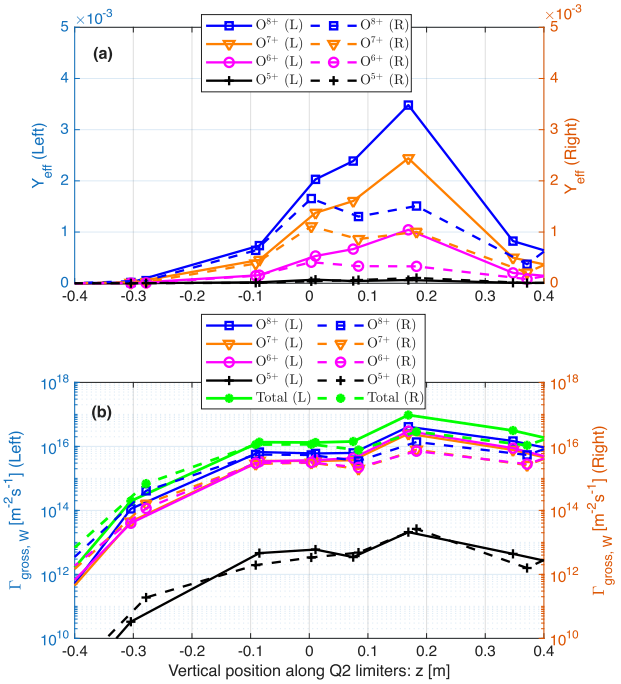

Figure 10. LOS-averaged vertical profiles during ICRH phase with thermal sheath only: (a) Y_{eff}; (b) $\Gamma_{\text{gross,W}}$. The R limiter exhibits a central peak in yield, while the L limiter shows a slight vertical offset.

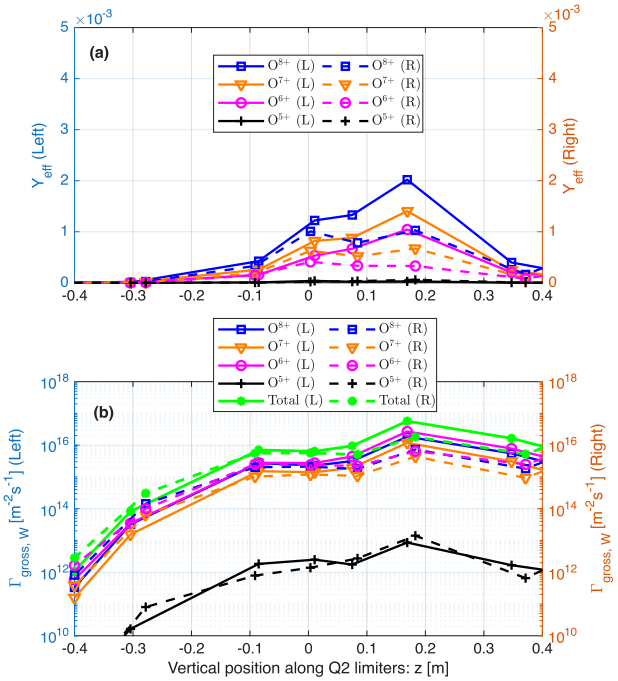

Figure 11. LOS-averaged vertical profiles during the ohmic phase (thermal sheath only): (a) Y_{eff}; (b) $\Gamma_{\text{gross,W}}$. Erosion levels are low with no midplane suppression. The L and R limiter profiles are broadly similar, though slight asymmetries appear near the peaks.

Toroidal Trends: The L limiter continues to exhibit slightly higher erosion than the R limiter in ohmic phase too. This asymmetry is more in the upper region of the limiter as can also be inferred from the Y_{eff} plot.

3.4 Validation Against Experimental Brightness

To enable direct comparison with experimental W-I spectroscopy, STRIPE computes synthetic brightness using charge-resolved $\Gamma_{\text{gross,W}}$ and S/XB coefficients obtained from ColRadPy [16]. The conversion from $\Gamma_{\text{gross,W}}$ to brightness $I_{\phi,\text{W-I}}$ is given by:

$$I_{\phi,\text{W-I}} = \frac{1}{A} \int \frac{\Gamma_{\text{gross,W}}}{4\pi\, \text{S/XB}}\, dA\,, \tag{6}$$

where A is the optical collection area, which is set based on a diagnostic radius of 90 mm, following [24]. This formulation provides a consistent synthetic diagnostic for comparing modeled erosion-driven emission with measured brightness profiles.

Figures 12 and 13 compare STRIPE-simulated and experimentally measured W-I 400.9 nm brightness profiles along the Q2 antenna limiters during ICRH and ohmic phases respectively. The comparison addresses spatial trends, asymmetries, and total integrated brightness.

During the ICRH phase (Figure 12), the experimental brightness profile peaks near the midplane (z = 0) and displays a broad, vertically extended distribution along both L and R limiters. In contrast, STRIPE predicts a strongly localized emission peak near the upper limiter region (z ∼ 0.34 m) and a pronounced dip at the midplane. This spatial discrepancy stems from the modeled localization of RF sheath potentials and impurity fluxes, which diverges from the experimentally observed emission structure. While STRIPE reproduces the overall brightness magnitude reasonably well, it does not capture a significant toroidal asymmetry in W erosion between the L and R limiters. In contrast, experimental measurements show consistently higher brightness on the R limiter, particularly near the midplane, indicating notable mismatches in both toroidal and poloidal distribution. Although STRIPE shows reasonable agreement with the measured profile on the L limiter, it significantly underpredicts emission on the R side—by a factor of 10–20 in the central region. Potential contributors to this discrepancy include $\mathbf{E} \times \mathbf{B}$ convection, RF field phasing, asymmetries in impurity sources, and reflections within the diagnostic line of sight, as discussed further in Section 4.

During the ohmic phase (Figure 13), both STRIPE and experimental measurements exhibit vertically symmetric brightness profiles with a slight upward shift and a clear peak near $z \sim 0.18$ m. The modeled $I_{\phi,\text{W-I}}$ closely reproduces the experimental trend, accurately capturing the peak location and the gradual decline toward the lower limiter region. Agreement is particularly strong on the R limiter, where discrepancies remain within a factor of two across the profile. Moreover, no significant toroidal asymmetry is observed in either the model or the experiment during this phase. The absence of RF sheath potentials leads to smoother brightness gradients and reduced overall intensity compared to the ICRH phase. This consistency

affirms the accuracy of STRIPE's charge-resolved impurity transport and thermal sheath modeling in non-RF conditions and further confirms that both poloidal and toroidal asymmetries in W erosion—more pronounced experimentally during ICRH—are primarily driven by RF sheath effects.

A summary of integrated W-I brightness $I_{\phi,\text{total}}$, computed from STRIPE is provided in Table 1. The total modeled brightness agrees with experimental values within 5% in the ohmic phase and within 30% during ICRH with RF sheath, supporting STRIPE's predictive fidelity and confirming the dominant role of O^{8+} and O^{7+} in RF-enhanced sputtering. Contributions from D^+ are negligible in all cases.

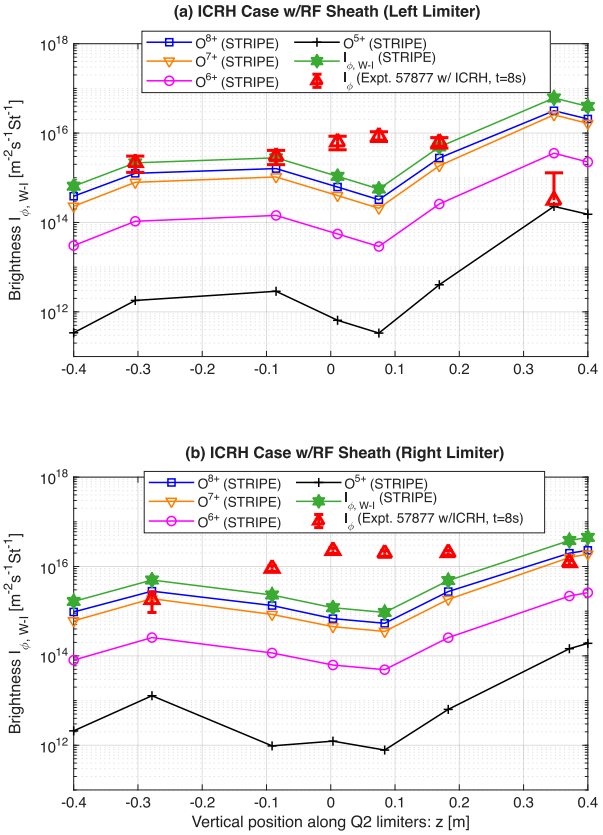

Figure 12. Comparison of STRIPE-simulated and experimental brightness profiles $I_{\phi,W-I}$ during ICRH with RF sheath. STRIPE predicts upper-limiter localization and L-dominant asymmetry, while the experiment shows midplane peaking and stronger brightness on the R side.

4 Discussion and Summary

This study applies the STRIPE framework to model impurity-driven W erosion at the WEST ICRH antenna during both ICRH and ohmic phases. STRIPE integrates 2D SolEdge3x plasma backgrounds, full-wave RF sheath potentials from COMSOL, charge-resolved ion transport via GITR, and sputtering yields from RustBCA.

As noted in Section 2, simulations interpreting the WEST ICRH discharge #57877 assume a 1% oxygen concentration as a proxy for light impurities. This choice, motivated by prior spectroscopic studies and edge modeling from previous WEST campaigns [9, 18], provides reasonable agreement with observed edge power balance and impurity fluxes despite the lack of charge-resolved measurements for this specific discharge. In reality, the impurity mix in WEST typically includes boron, nitrogen, carbon, and W itself in addition to oxygen. These species will be incorporated in future modeling to refine predictions of radiative losses and sputtering behavior.

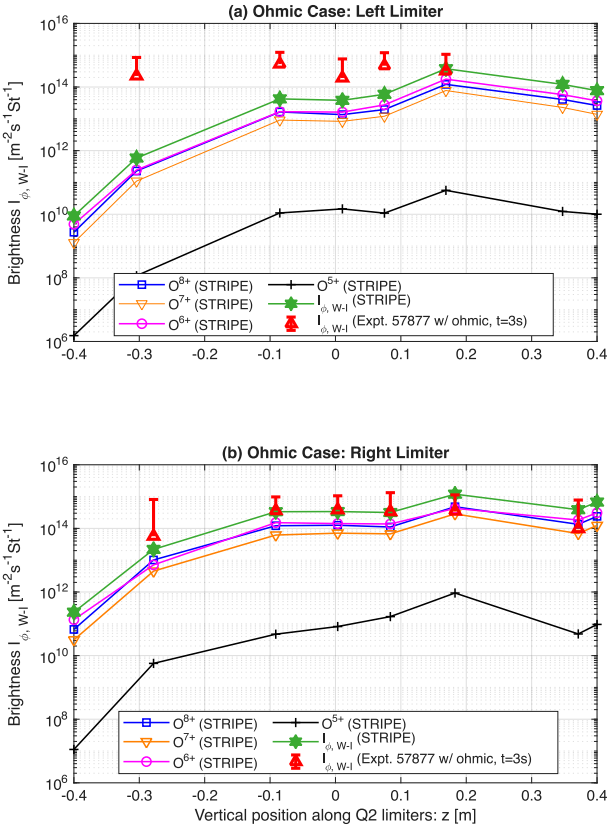

Figure 13. Comparison of STRIPE-simulated and experimental brightness profiles $I_{\phi,W-I}$ during the ohmic phase. Both model and experiment show vertically uniform emission and toroidal symmetry.

Simulations reveal that rectified RF sheath potentials substantially amplify gross W erosion, increasing $\Gamma_{\text{gross,W}}$ by more than an order of magnitude compared to thermal sheaths and by over 30× relative to the ohmic case. This enhancement is driven by elevated sheath voltages (up to 300 V) that energize high-charge-state oxygen ions (O^{6+}–O^{8+}), which dominate the sputtering response. D^+ contributes negligibly.

Erosion is poloidally localized near the upper limiter region, in line with the modeled distribution of RF sheath potentials and impurity fluxes. Toroidally, STRIPE predicts relatively symmetric erosion due to the assumed axisymmetric plasma background. However, experimental W-I brightness during ICRH shows stronger emission on the R limiter and a peak near the midplane, highlighting a discrepancy in both toroidal and poloidal behavior. In

Table 1. Simulated charge-resolved W photon brightness I_ϕ [photons/s] and comparison with experiment.

Case	O^{8+}	O^{7+}	O^{6+}	O^{5+}	D^+	**Total** $I_{\phi,\text{total}}$	**Experiment**
RF (ICRH)	2.26×10^{16}	1.68×10^{16}	4.02×10^{15}	1.11×10^{14}	9.67×10^{10}	4.35×10^{16}	3.38×10^{16}
Thermal (ICRH)	1.93×10^{15}	1.10×10^{15}	2.58×10^{14}	8.95×10^{13}	0	3.29×10^{15}	–
Thermal (Ohmic)	8.05×10^{14}	4.86×10^{14}	6.45×10^{13}	2.66×10^{13}	0	1.39×10^{15}	1.32×10^{15}

contrast, during the ohmic phase, both model and experiment exhibit vertically symmetric brightness profiles with peaks near $z \sim 0.18$ m, showing agreement within a factor of two—supporting the validity of STRIPE in non-RF conditions.

Our current STRIPE modeling does not include cross-field $\mathbf{E} \times \mathbf{B}$ convection. However, COMSOL-derived RF sheath potentials (Fig. 6) exhibit strong poloidal gradients, particularly in the upper limiter region ($z > 0$), with peak voltages exceeding 250 V. These gradients can generate radial electric fields and drive $\mathbf{E} \times \mathbf{B}$ flows toward the midplane ($z \approx 0$), potentially enhancing local plasma density and impurity fluxes [25]. This mechanism may contribute to the midplane erosion peak observed experimentally, which is not reproduced by the STRIPE modeling. Including this physics in future STRIPE versions could improve agreement with experiment and better resolve poloidal asymmetries in impurity dynamics.

The mismatch in toroidal asymmetry during ICRH may also stem from unmodeled 3D plasma features, RF sheath model limitations, or line-of-sight diagnostic effects. A slight radial misalignment between limiters due to mechanical tolerances could also contribute. Additionally, optical modeling [26] suggests that W-I brightness measurements may be inflated by reflections from metallic PFCs, contributing up to 95% of the signal—potentially explaining the brightness excess observed experimentally.

Nonetheless, the upper-limiter erosion enhancement predicted by STRIPE aligns with recent WEST discharges [27] and AUG ICRH observations [28], reaffirming RF sheath rectification as a primary driver of localized erosion.

Although the simulations and diagnostics presented here primarily emphasize localized erosion at the antenna, Figure 3 also provides information on global W sourcing. In particular, Fig. 3(a) shows that the radiated power fraction $P_{\text{rad}}/P_{\text{in}}$ remains nearly constant between the ohmic and ICRH phases. However, Fig. 3(b) reveals that antenna W-I brightness rises by over 25× during ICRH—closely matching the $\sim$ 30× increase in erosion predicted by STRIPE—while emission from the inner divertor vanishes (consistent with detachment) and the outer divertor shows only a transient peak before decaying. The sustained antenna signal underscores the role of RF sheath-driven erosion, while the reduction of divertor sources is consistent with recent WEST studies [17] showing that ICRF application can redistribute W sourcing. As a result, main chamber sources, especially near the antenna, can dominate the W balance.

These opposing source trends may cancel in their radiative signature, explaining why $P_{\text{rad}}/P_{\text{in}}$ remains flat despite large local variations. Moreover, recent WEST experiments indicate that main chamber contributions dominate the core W balance under ICRF conditions. Therefore, $P_{\text{rad}}/P_{\text{in}}$ is not a reliable indicator of RF-induced W erosion. Taken together, these results highlight the importance of spatially resolved diagnostics and global impurity transport simulations to capture W sourcing, redistribution, and accumulation across the W-PFC environment.

Furthermore, the present study highlights that the magnitude of ICRH-driven W erosion is highly sensitive to the concentration of light impurities (O, B, N, C, etc.), whose high charge states drive efficient sputtering. Achieving cleaner plasma conditions with reduced levels of these species is therefore expected to significantly mitigate antenna-related tungsten sources in WEST and other toroidal fusion devices.

Overall, STRIPE provides a validated and extensible platform for analyzing RF-induced plasma–material interactions in reactor-relevant scenarios. Future developments will address net erosion, re-deposition, and whole-device impurity transport. Planned validation activities include benchmarking COMSOL-predicted sheath potentials with emissive probe measurements, simulating D I line emission to better constrain input n_e and T_e, and modeling mixed light impurity species.

In addition to global impurity transport and $\mathbf{E} \times \mathbf{B}$ convection, methodological upgrades will also include incorporation of DC plasma conductivity into the rectification model. These advances will be supported by coupling 3D SolEdge3x with COMSOL, together with GITRm for global impurity transport, enabling self-consistent modeling of RF sheath dynamics and whole-device impurity behavior.

Acknowledgement

This work was supported by the U.S. Department of Energy (DOE) Office of Science, through the SciDAC program and utilized resources from the Fusion Energy Division and ORNL Research Cloud under Contract No. DE-AC05-00OR22725. Work at PPPL was supported by DOE Contract No. DE-AC02-09CH11466.

References

[1] M. Maslov, E. Lerche, F. Auriemma, E. Belli, C. Bourdelle, C. Challis, A. Chomiczewska, A.D. Molin, J. Eriksson, J. Garcia et al., JET D-T scenario with optimized non-thermal fusion, Nuclear Fusion **63**, 112002 (2023). https://doi.org/10.1088/1741-4326/ace2d8

[2] A.J. Creely, M.J. Greenwald, S.B. Ballinger, D. Brunner, J. Canik, J. Doody, T. Fülöp,

D.T. Garnier, R. Granetz, T.K. Gray et al., Overview of the SPARC tokamak, Journal of Plasma Physics **86**, 865860502 (2020). https://doi.org/10.1017/S0022377820001257

[3] W. Tierens, A. Kumar, C. Klepper, J. Lore, J. Myra, J. Hillairet, G. Urbanczyk, W. Helou, L. Colas, A. Grosjean et al., Radiofrequency sheath rectification on WEST: application of the sheath-equivalent dielectric layer technique in tokamak geometry, Nuclear Fusion **64**, 126039 (2024). https://doi.org/10.1088/1741-4326/ad80a9

[4] L. Colas, W. Helou, G. Urbanczyk, V. Bobkov, F. Calarco, N. Fedorczak, D. Milanesio, J. Hillairet, Numerical assessment of ICRF-specific plasma-wall interaction in the new ITER baseline using the SSWICH-SW code, Nuclear Materials and Energy **42**, 101831 (2025). https://doi.org/10.1016/j.nme.2024.101831

[5] L. Colas, G. Urbanczyk, M. Goniche, J. Hillairet, J.M. Bernard, C. Bourdelle, N. Fedorczak, C. Guillemaut, W. Helou, V. Bobkov et al., The geometry of the ICRF-induced wave–SOL interaction. a multi-machine experimental review in view of the ITER operation, Nuclear Fusion **62**, 016014 (2021). https://doi.org/10.1088/1741-4326/ac35f9

[6] V. Bobkov, D. Aguiam, R. Bilato, S. Brezinsek, L. Colas, H. Faugel, H. Fünfgelder, A. Herrmann, J. Jacquot, A. Kallenbach et al., Making icrf power compatible with a high-z wall in asdex upgrade, Plasma Physics and Controlled Fusion **59**, 014022 (2016). https://doi.org/10.1088/0741-3335/59/1/014022

[7] F. Waelbroeck, J. Winter, G. Esser, B. Giesen, L. Konen, V. Philipps, U. Samm, J. Schluter, P. Weinhold, T.T. Team et al., Influence of boronization on the plasma performance in TEXTOR, Plasma Physics and Controlled Fusion **31**, 185 (1989). https://doi.org/10.1088/0741-3335/31/2/004

[8] S.J. Wukitch, M.L. Garrett, R. Ochoukov, J.L. Terry, A. Hubbard, B. Labombard, C. Lau, Y. Lin, B. Lipschultz, D. Miller et al., Characterization and performance of a field aligned ion cyclotron range of frequency antenna in Alcator C-Mod), Physics of Plasmas **20**, 056117 (2013). https://doi.org/10.1063/1.4803882

[9] C.C. Klepper, E.A. Unterberg, Y. Marandet, D. Curreli, A. Grosjean, J.H. Harris, C.A. Johnson, A. Gallo, M. Goniche, C. Guillemaut et al., Characterizing W sources in the all-W wall, all-RF WEST tokamak environment, Plasma Physics and Controlled Fusion **64**, 104008 (2022). https://doi.org/10.1088/1361-6587/ac8acc

[10] W. Zhang, R. Bilato, V. Bobkov, A. Cathey, A. Di Siena, M. Hoelzl, A. Messiaen, J. Myra, G. Suárez López, W. Tierens et al., Recent progress in modeling ICRF-edge plasma interactions with application to ASDEX Upgrade, Nuclear Fusion **62**, 075001 (2022). https://doi.org/10.1088/1741-4326/ac38c8

[11] A. Kumar, W. Tierens, T. Younkin, C. Johnson, C. Klepper, A. Diaw, J. Lore, A. Grosjean, G. Urbanczyk, J. Hillairet et al., Integrated modeling of RF-induced tungsten erosion at ICRH antenna structures in the WEST tokamak, Nuclear Fusion **65**, 076039 (2025). https://doi.org/10.1088/1741-4326/ade455

[12] R. Dumont, et. al., RF power experiments in WEST to prepare for next-step fusion device operation, in *25th Topical Conference on Radio-Frequency Power in Plasmas* (2025), invited paper, Hohenkammer, Germany, 19–22 May 2025, https://www.ipp.mpg.de/5487515/Talks

[13] H. Bufferand, G. Ciraolo, Y. Marandet, J. Bucalossi, P. Ghendrih, J. Gunn, N. Mellet, P. Tamain, R. Leybros, N. Fedorczak et al., Numerical modelling for divertor design of the WEST device with a focus on plasma–wall interactions, Nuclear Fusion **55**, 053025 (2015). https://doi.org/10.1088/0029-5515/55/5/053025

[14] T. Younkin, D. Green, A. Simpson, B. Wirth, Gitr: An accelerated global scale particle tracking code for wall material erosion and redistribution in fusion relevant plasma–material interactions, Computer Physics Communications **264**, 107885 (2021). https://doi.org/10.1016/j.cpc.2021.107885

[15] J. Drobny, D. Curreli, Rustbca: A high-performance binary-collision-approximation code for ion-material interactions, Journal of Open Source Software **6**, 03298 (2021). https://doi.org/10.21105/joss.03298

[16] C. Johnson, S. Loch, D. Ennis, Colradpy: A python collisional radiative solver, Nuclear Materials and Energy **20**, 100579 (2019). https://doi.org/10.1016/j.nme.2019.01.013

[17] L. Colas et al., Tungsten gross erosion and plasma impurity contamination in WEST Phase 1: a statistical comparison of LH and ICRF-heated L-mode plasmas, in *29th IAEA Fusion Energy Conference (IAEA–CN–316)* (London, United Kingdom, 2023), paper IAEA–CN–316-2045

[18] G. Ciraolo, A. Thin, H. Bufferand, J. Bucalossi, N. Fedorczak, J. Gunn, J. Pascal, P. Tamain, C. Gil, A. Gouin et al., First modeling of strongly radiating WEST plasmas with SOLEDGE-EIRENE, Nuclear Materials and Energy **20**, 100685 (2019). https://doi.org/10.1016/j.nme.2019.100685

[19] R. Diab, et.al., Direct measurements of rf sheath potentials in WEST using a reciprocating emissive probe, Presented at the 25th Topical Conference on Radio Frequency Power in Plasmas (RFPPC) (2025), invited paper, Hohenkammer, Germany, 19–22 May 2025, https://www.ipp.mpg.de/5487515/Talks

[20] G. Urbanczyk, R. Ochoukov, V. Bobkov, S. Shiraiwa, R. Bilato, N. Bertelli, W. Tierens, L. Colas, R. Dux, M. Dreval et al., Characterization of w production during icrf operations: experiments and modeling, Nuclear Fusion **65**, 046018 (2025). https://doi.org/10.1088/1741-4326/adbd52

[21] J.N. Brooks, Near-surface sputtered particle transport for an oblique incidence magnetic field plasma, Physics of Fluids B: Plasma Physics **2**, 1858 (1990). https://doi.org/10.1063/1.859457

[22] P.C. Stangeby, The Plasma Boundary of Magnetic Fusion Devices (1st ed.) (CRC Press, 2000)

[23] R. Khaziev, D. Curreli, hpic: A scalable electrostatic particle-in-cell for plasma–material interactions, Computer Physics Communications **229**, 87 (2018). https://doi.org/10.1016/j.cpc.2018.03.028

[24] O. Meyer, J.C. Giacalone, A. Gouin, J.Y. Pascal, C.C. Klepper, N. Fedorczak, P. Lotte, E.A. Unterberg, D.T. Fehling, J.H. Harris et al., Visible spectroscopy diagnostics for tungsten source assessment in the WEST tokamak: First measurements, Review of Scientific Instruments **89**, 10D105 (2018). https://doi.org/10.1063/1.5035566

[25] W. Zhang, W. Tierens, J.M. Noterdaeme, V. Bobkov, D. Aguiam, D. Coster, H. Fuenfgelder, J. Jacquot, R. Ochoukov, A. Silva et al., Radio frequency heating induced edge plasma convection: self-consistent simulations and experiments on ASDEX Upgrade, Nuclear Fusion **57**, 116048 (2017). https://doi.org/10.1088/1741-4326/aa7f47

[26] C.A. Johnson, A. Diaw, E.A. Unterberg, N. Fedorczak, P. Tamain, Analyzing the effects of reflections on optical diagnostics in the main chamber and divertor of WEST, Review of Scientific Instruments **95**, 123505 (2024). https://doi.org/10.1063/5.0219546

[27] W. Tierens, A. Kumar, J. Lore, G. Urbanczyk, R. Diab, the WEST Team, Gyrotropy-induced symmetry breaking of erosion hot spots on antenna limiters during high-power tokamak rf operation: Mechanisms and mitigation strategies, arXiv preprint arXiv:2508.02445 (2025). https://doi.org/10.48550/arXiv.2508.02445

[28] V. Bobkov, F. Braun, R. Dux, L. Giannone, A. Herrmann, A. Kallenbach, H. Müller, R. Neu, J.M. Noterdaeme, T. Pütterich et al., Operation of ICRF antennas in a full tungsten environment in ASDEX Upgrade, Journal of Nuclear Materials **390-391**, 900 (2009). https://doi.org/10.1016/j.jnucmat.2009.01.231